ELSEVIER

Full length article

Multiscale characterization of heart failure

F. Sahli Costabal [a], J.S. Choy [b], K.L. Sack [c], J.M. Guccione [d], G.S. Kassab [b], E. Kuhl [a,*]

[a] *Departments of Mechanical Engineering & Bioengineering, Stanford University, CA, USA*
[b] *California Medical Innovations Institute, Inc., San Diego, CA, USA*
[c] *Department of Human Biology, University of Cape Town, Cape Town, South Africa*
[d] *Department of Surgery, University of California at San Francisco, San Francisco, CA, USA*

ABSTRACT

Dilated cardiomyopathy is a progressive irreversible disease associated with contractile dysfunction and heart failure. During dilated cardiomyopathy, elevated diastolic wall strains trigger mechanotransduction pathways that initiate the addition of sarcomeres in series and an overall increase in myocyte length. At the whole organ level, this results in a chronic dilation of the ventricles, an increase in end diastolic and end systolic volumes, and a decrease in ejection fraction. However, how exactly changes in sarcomere number translate into changes in myocyte morphology, and how these cellular changes translate into ventricular dilation remains incompletely understood. Here we combined a chronic animal study, continuum growth modeling, and machine learning to quantify correlations between sarcomere dynamics, myocyte morphology, and ventricular dilation. In an eight-week long volume overload study of six pigs, we found that the average sarcomere number increased by +3.8%/week, from 47 to 62, resulting in a myocyte lengthening of +3.3%/week, from 85 to 108 μm, while the sarcomere length and myocyte width remained unchanged. At the same time, the average end diastolic volume increased by +6.0%/week. Using continuum growth modeling and Bayesian inference, we correlated alterations on the subcellular, cellular, and organ scales and found that the serial sarcomere number explained 88% of myocyte lengthening, which, in turn, explained 54% of cardiac dilation. Our results demonstrate that sarcomere number and myocyte length are closely correlated and constitute the major determinants of dilated heart failure. We anticipate our study to be a starting point for more sophisticated multiscale models of heart failure. Our study suggests that altering sarcomere turnover-and with it myocyte morphology and ventricular dimensions-could be a potential therapeutic target to attenuate or reverse the progression of heart failure.

Statement of Significance

Heart failure is a significant global health problem that affects more than 25 million people worldwide and increases in prevalence as the population ages. Heart failure has been studied excessively at various scales; yet, there is no compelling concept to connect knowledge from the subcellular, cellular, and organ level *across* the scales. Here we combined a chronic animal study, continuum growth modeling, and machine learning to quantify correlations between sarcomere dynamics, myocyte morphology, and ventricular dilation. We found that the serial sarcomere number explained 88% of myocyte lengthening, which, in turn, explained 54% of cardiac dilation. Our results show that sarcomere number and myocyte length are closely correlated and constitute the major determinants of dilated heart failure. This suggests that altering the sarcomere turnover—and with it myocyte morphology and ventricular dimensions– could be a potential therapeutic target to attenuate or reverse heart failure.

1. Introduction

Heart disease is the leading cause of death and disability worldwide, accounting for 40% of all human mortality. More than six million Americans suffer from heart failure associated with a very high mortality and poor quality of life [44]. With one million new cases diagnosed each year, heart failure generates an annual health care cost in excess of 30 billion [1]. Cardiac dilation in heart failure has been the subject of extensive research at different scales throughout the past decades [53]; yet, to date, there is no

* Corresponding author.
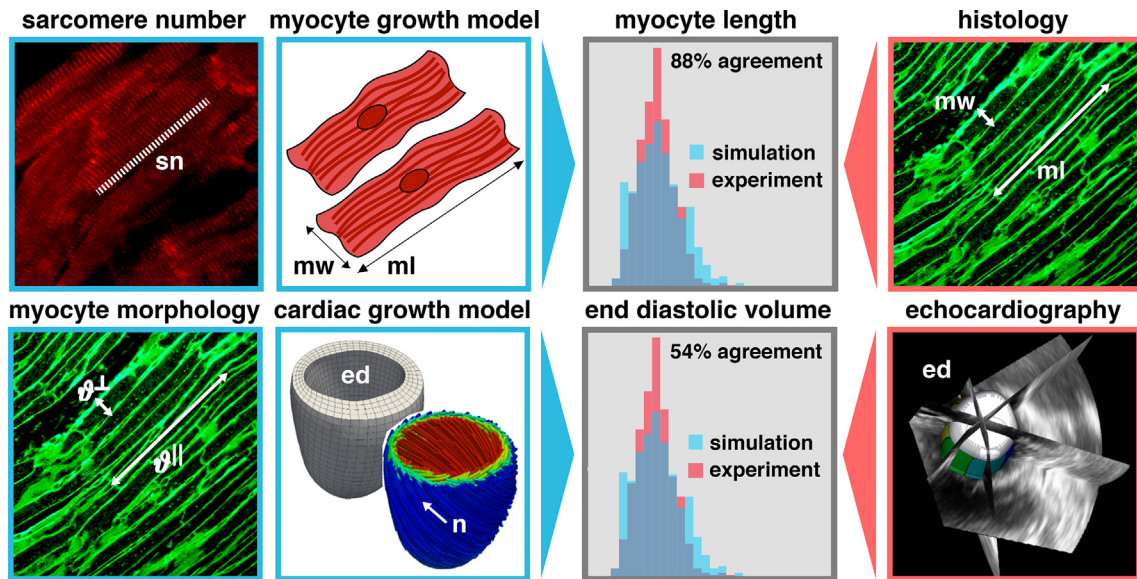*E-mail address:* ekuhl@stanford.edu (E. Kuhl).

Fig. 1. Bridging the subcellular, cellular, and tissue levels using a multiscale continuum growth model. We characterize sarcomere numbers and length, myocyte widths and lengths, and end diastolic and systolic volumes in a longitudinal study of volume overload using histology and echocardiography. We quantify the agreement between simulation and experiment in terms of myocyte lengths and end diastolic volumes recorded in six animals throughout a period of eight weeks.

compelling concept to connect knowledge from the subcellular, cellular, and organ level *across* the scales.

Unlike many other cell types in the human body, adult heart muscle cells, cardiomyocytes, do not multiply by cell division. It is a widely accepted paradigm that the total number of cardiomyocytes – about 6 billion at birth-does not increase throughout an individual's life time [31]. However, cardiomyocytes can grow in size. They do so through sarcomerogenesis, the creation and deposition of new sarcomere units [29]. Sarcomeres, the functional contractile units of cardiac cells, are characterized through a 1.7–2.1 μm long parallel arrangement of thick filaments of myosin that slide along thin filaments of actin [3]. Approximately 50 sarcomeres in series make up a myofibril; about 50–100 myofibrils in parallel make up a cardiomyocyte [50]. Healthy cardiomyocytes have a cylindrical shape with a length of approximately 80–100 μm and a diameter of 10–25 μm [36].

Cardiomyocyte morphology exhibits distinct variations under various pathological conditions [33]. In response to a chronic volume overload, elevated diastolic wall strains on the whole heart scale translate into a stretching of cardiomyocytes on the cellular scale which results in an increase in sarcomere length on the subcellular scale [45]. Sarcomeres are known to operate at a tightly regulated optimal length [34], an observation that is known as the Frank-Starling mechanism [9,52]. Any deviation away from this length is associated with a loss of function [21]. Elevated diastolic wall strains trigger mechanotransduction pathways that initiate the addition of sarcomeres in series [19] and an overall increase in cardiomyocyte length [37]. At the whole organ level, this results in a chronic dilation of the ventricle, an increase in end diastolic and end systolic volumes, and a decrease in ejection fraction [12]. However, how exactly changes in sarcomere number translate into changes in cardiomyocyte morphology, and how these cellular changes translate into ventricular dilation is insufficiently understood.

Multiscale modeling provides a powerful concept to integrate knowledge from different scales and correlate molecular and cellular structure to whole organ function. The objective of this study was to synthesize the information from three biological scales and establish mechanistic links between them using a chronic animal study, continuum growth modeling, and machine learning.

We tested the hypothesis that chronic overstretch induces the addition of sarcomeres on the subcellular scale, which translates into progressive cell lengthening on the cellular scale, and results in cardiac dilation on the organ scale. Specifically, we performed an eight-week long volume overload study in pigs to quantify exactly to which extent changes in myocyte morphology can explain ventricular dilation in heart failure.

2. Materials and methods

Fig. 1 outlines the methods used in this study. We correlate the subcellular, cellular, and tissue levels using a multiscale continuum growth model. We characterize sarcomere numbers and length, myocyte widths and lengths, and end diastolic and systolic volumes in a longitudinal study of volume overload using histology and echocardiography. We quantify the agreement between simulation and experiment in terms of myocyte lengths and end diastolic volumes recorded in six animals throughout a period of eight weeks.

2.1. Volume overload model

All animal experiments were performed in accordance with national and local ethical guidelines, including the Guide for the Care and Use of Laboratory Animals, the Public Health Service Policy on Humane Care and Use of Laboratory Animals, and the Animal Welfare Act, and an approved California Medical Innovations Institute IACUC protocol. As previously described [6], we used six Yorkshire domestic pig of either sex with a body weight of 46.3 ± 8.0 kg and housed the animals at the California Medical Innovations Institute animal care facilities. At the day of surgery, we performed sedation with telazol-ketamine-xylazine and maintained anesthesia with isoflurane. Under sterile conditions, we percutaneously inserted sheaths into the jugular vein to administer fluids and drugs and into the right femoral artery, to monitor the pressure, and to provide access to the left ventricle for mitral valve chordae disruption. Under fluoroscopic guidance, we advanced a shapeable biopsy forceps towards the anterolateral wall of the left ventricle near the base of the heart. Using transesophageal

echocardiography guidance, we created moderate to severe regurgitation by disrupting one or more chordae. Using echocardiography, we confirmed that the degree of mitral regurgitation was similar in all the animals. At the end of the eight-week long study, we deeply anesthetized the animal, arrested the heart in diastole with potassium chloride, and excised it. Finally, we collected transmural punch biopsy samples from the apex and free wall.

2.2. Cell level characterization – histology

For the cell level characterization, we collected endomyocardial biopsy samples at baseline at the day of mitral valve chordae disruption and at bi-weekly follow-up for a total of eight weeks. Under fluoroscopic guidance, we advanced a shapeable biopsy forceps into the left ventricle where we collected four to six endomyocardial samples from the apical region and from the free wall. To minimize variations in the state of contraction, we incubated the samples in cardioplegic solution at 37 °C before routine histological processing. We aligned the plane of the samples parallel to the longitudinal axis of the myocardial fiber and embedded them in tissue freezing medium. We prepared 7-µm-thick slices and mounted them on glass slides. We incubated them with Wheat Germ Agglutinin, Alexa Fluor 488 Conjugate, Thermo Fisher Scientific to characterize myocyte dimensions and with Anti-Sarcomeric Alpha Actinin to identify the individual sarcomeres. Under fluorescence microscopy, we merged the images using ImageJ to identify the sarcomere numbers within each myocyte. We surveyed non-repeating fields for myocytes in their longitudinal axis, with no tears or sectioning artifacts, and excluded myocytes that did not meet these criteria from our analysis. In this study, we focus on quantifying myocyte dimensions; in the future, we will also quantify the percentage of fibrotic tissue in the tissue sections. Fig. 2 illustrates our cell level characterization of healthy myocytes at baseline and of volume overloaded myocytes at week 8. Table 6 in the Appendix provides an overview of the number of sarcomere numbers, sarcomere lengths, myocyte lengths, and myocyte widths we recorded for each animal at each time point.
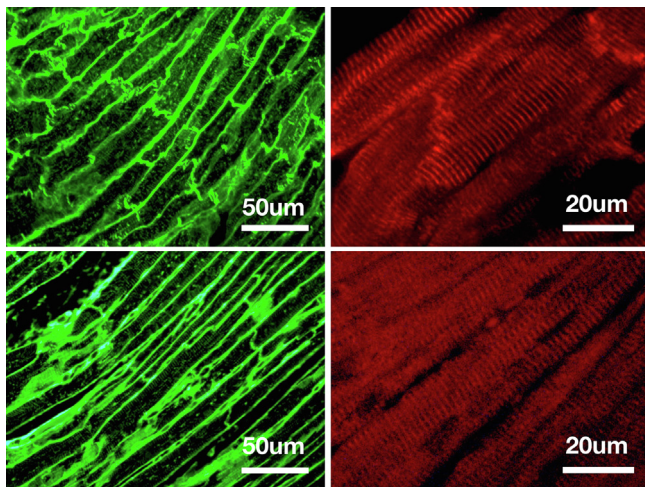

Fig. 2. Changes in histology in response to left ventricular volume overload. Healthy myocytes, top, at baseline were 85.45 ± 22.30 µm long and 13.67 ± 3.73 µm wide, made up of 47.50 ± 11.67 sarcomeres with a length of 1.75 ± 0.15 µm. Volume overloaded myocytes at week 8, bottom, were 107.75 ± 26.57 µm long and 12.98 ± 3.01 µm wide, made up of 62.07 ± 16.35 sarcomeres with a length of 1.77 ± 0.11 µm.

2.3. Organ level characterization – echocardiography

For the organ level characterization, we recorded transthoracic and transesophageal echocardiograms at baseline at the day of mitral valve chordae disruption and at bi-weekly follow-up for a total of eight weeks. We acquired all echocardiographic images, two- and three-dimensional in short and long axis views, with the animal placed in the supine and left lateral decubitus positions. From these images, we calculated the left ventricular end-diastolic volumes, end-systolic volumes, stroke volumes, ejection fractions, and wall thicknesses. We performed an offline three-dimensional volumetric analysis using the TomTec 4D LV-Function, Version 4.6, Build 4.6.3.9, Unterschleissheim, Germany. Briefly, we marked the positions of the mitral valve and the apex in each of the apical planes and manually delineated the endocardial borders at end-diastole. The software then automatically traced the contours dynamically throughout the cardiac cycle. If necessary, we performed manual corrections in both end-diastolic and end-systolic frames to include the papillary muscles and trabeculae. From the automatically constructed dynamic surface models of the left ventricle, we extracted end diastolic and systolic volumes and ejection fractions.

2.4. Data analysis

To analyze the changes in both microscopic and macroscopic variables in all subjects, we employed Bayesian inference. For all recorded samples, we postulated that our measurements are drawn from distributions that evolve over time. Specifically, we assumed that the measurements of sarcomere number and length, myocyte length and width, and end diastolic and systolic volumes are log-normally distributed at any point in time. We chose this particular distribution to ensure that all samples generated from these distributions are strictly positive. For the myocyte length and width, we further postulated that these two quantities are correlated, and assumed a bivariate log-normal likelihood,

$$\begin{bmatrix} \log(y_{\mathrm{ml}}^{ij}) \\ \log(y_{\mathrm{mw}}^{ij}) \end{bmatrix} \sim \mathcal{N}\left(\begin{bmatrix} \mu_{\mathrm{ml}}^i(t_j) \\ \mu_{\mathrm{mw}}^i(t_j) \end{bmatrix}, \Sigma \right), \quad (1)$$

where y_{ml}^{ij} and y_{mw}^{ij} represent the measurement j of subject i of myocyte length ml and myocyte width mw, $\mu_{\mathrm{ml}}^i(t_j)$ and $\mu_{\mathrm{mw}}^i(t_j)$ are the means of their distributions at the time of measurement j, and Σ is the co-variance matrix between these quantities. For the remaining quantities, we assumed a simple log-normal likelihood,

$$\log(y_{\mathrm{k}}^{ij}) \sim \mathcal{N}(\mu_{\mathrm{k}}^i(t_j), \sigma_{\mathrm{k}}) \quad \text{with} \quad \mathrm{k} = \{\mathrm{sn, sl, ed}\}, \quad (2)$$

where y_{k}^{ij} is the measurement j of subject i of quantity k, either sarcomere number sn, sarcomere length sl, or end diastolic volume ed, $\mu_{\mathrm{k}}^i(t_j)$ is the mean of its distribution at time of measurement j for the quantity k and, σ_{k} is the standard deviation for the quantity k. We adopted the simplest relationship between the mean and time,

$$\mu_{\mathrm{k}}^i(t) = a_{\mathrm{k}}^i + b_{\mathrm{k}}^i t \quad \text{with} \quad \mathrm{k} = \{\mathrm{ml, mw, sn, sl, ed}\}. \quad (3)$$

Here a_{k}^i and b_{k}^i represent the intercept and slope of the line $\mu(t)$ for subject i and quantity k. To take into account the variability between subjects and, at the same time, take advantage of the entire acquired dataset, we postulated a hierarchical model [11]. Specifically, we assumed that the different parameters of the model in Eq. (3) $a_{\mathrm{k}}^i \sim \mathcal{N}(\mu_{\mathrm{k}}^a, \sigma_{\mathrm{k}}^a)$ and $b_{\mathrm{k}}^i \sim \mathcal{N}(\mu_{\mathrm{k}}^b, \sigma_{\mathrm{k}}^b)$ for each subject i are drawn from normal distributions. With this approach, we introduced four hyper-parameters for each quantity k, $\mu_{\mathrm{k}}^a, \mu_{\mathrm{k}}^b, \sigma_{\mathrm{k}}^a$ and σ_{k}^b, which control the variability between the parameters a_{k}^i and

b_k^i for each subject i. This allowed us to estimate the individual responses for each subject in view of the totality of the cohort. The last step to completely specify the statistical model in a Bayesian setting was to set the prior distributions. These encode our previous knowledge about the parameters. In our case, we used weakly informative priors to ensure a small influence in the posterior distributions. For the hyper-parameters we chose $\mu_k^a, \mu_k^b \sim \mathcal{N}(0, 100^2)$ and $\sigma_k^a, \sigma_k^b \sim \text{Half} - \text{Cauchy}(\gamma = 10)$ [10], and the prior distributions of the remaining parameters as $\sigma_k \sim \text{Half} - \text{Cauchy}(\gamma = 100)$, for $k = \{\text{sn}, \text{sl}, \text{ed}\}$ and $\Sigma \sim \text{LKJ}(\eta = 2)$, where LKJ denotes the Lewandowski-Kurowicka-Joe distribution [32]. This distribution is particularly suitable for multi-variate normal co-variance matrices [49]. Finally, we computed the posterior distributions for the parameters using Bayes' theorem. We performed the statistical inference using a Hamiltonian Monte Carlo method implemented in PyMC3 [49]. We then computed new samples of our quantities of interest y_k from a predictive posterior distribution at different time points and plotted the discrete measurement points, their medians, their 95% confidence intervals, and their inferred probability density functions throughout our study interval of eight weeks.

2.5. Correlating the subcellular, cellular, and organ levels

To correlate the subcellular and cellular scales, we assumed a linear relation between relative changes in the longitudinal sarcomere number and relative changes in myocyte length [59]. We correlated changes in myocyte morphology to the overall change in end diastolic volume using a transversely isotropic growth model [16,17] based on a second-order growth tensor,

$$\boldsymbol{F}^g = \vartheta^{\parallel} \boldsymbol{n} \otimes \boldsymbol{n} + \vartheta^{\perp} [\boldsymbol{I} - \boldsymbol{n} \otimes \boldsymbol{n}], \tag{4}$$

that directly correlates the scalar longitudinal and transverse growth multipliers $\vartheta^{\parallel}$ and $\vartheta^{\perp}$ to the relative changes in myocyte length and myocyte width along the fiber direction $\boldsymbol{n}$ [59].

Fig. 3 illustrates the kinematics of our multiscale growth model, with the deformation φ, the deformation gradient $\boldsymbol{F} = \nabla \boldsymbol{\varphi} = \boldsymbol{F}^e \cdot \boldsymbol{F}^g$, the elastic tensor $\boldsymbol{F}^e$, and the growth tensor $\boldsymbol{F}^g$, which is a direct result of the changes in myocyte length $\vartheta^{\parallel}$ and width $\vartheta^{\perp}$. From the echocardiography images of each animal, we created finite element models of the left ventricle at the minimum

Fig. 3. Correlating cellular and organ levels. Illustration of the deformation φ, deformation gradient $\boldsymbol{F} = \nabla \boldsymbol{\varphi} = \boldsymbol{F}^e \cdot \boldsymbol{F}^g$, elastic tensor $\boldsymbol{F}^e$, and growth tensor $\boldsymbol{F}^g$ to correlate changes in end diastolic volume to changes in myocyte length $\vartheta^{\parallel}$ and width $\vartheta^{\perp}$.

cavity volume of the cardiac cycle and assumed that this is the stress free state. Fig. 3 illustrates our left ventricular models that consist of 3456 linear hexahedral elements, 4152 nodes, and 12,456 degrees of freedom. We assigned each element a discrete fiber orientation $\boldsymbol{n}$ using a rule-based approach [30] in which the fiber angles vary from $+60^o$ in the endocardium to -60° in the epicardium, measured with respect to the horizontal plane [56]. For the baseline elastic material response, we adopted the classical Holzapfel-Ogden model [18,22],

$$\psi = \frac{a}{2b} \exp(b[I_1^e - 3]) + \frac{a_f}{2b_f} [\exp(b_f [I_{4f}^e - 1]^2) - 1]$$
$$+ \frac{a_s}{2b_s} \left[\exp(b_s [I_{4s}^e - 1]^2) - 1 \right] + \frac{a_{fs}}{2b_{fs}} \left[\exp(b_{fs} (I_{8fs}^e)^2) - 1 \right], \tag{5}$$

where $I_1^e, I_{4f}^e, I_{4s}^e$, and I_{8fs}^e are the invariants that characterize the trace of the right elastic Cauchy Green deformation tensor, the elastic fiber stretch, sheet stretch, and coupled fiber-sheet stretch. We calibrated the eight Holzapfel-Ogden material parameters $a, b, a_f, b_f, a_s, b_s, a_{fs}, b_{fs}$ individually for each animal [46] using the recorded end diastolic pressure and the Klotz curve [27]. We used the Abaqus explicit solver [7] and created the end diastolic state by inflating the ventricle with the end diastolic pressure. Then we gradually increased the growth tensor of Eq. (4) up to the prescribed longitudinal and transverse growth multipliers $\vartheta^{\parallel}$ and $\vartheta^{\perp}$. From the simulations, we extracted the progression of the cavity volume for varying growth multipliers.

2.6. Uncertainty propagation

To correlate the subcellular and cellular levels and the cellular and organ levels, we propagated the uncertainty of our experimental measurements through our computational models. To quantify the agreement, we compared the simulated and experimental myocyte lengths and end diastolic volumes using the overlap coefficient, which represents the percentage agreement between the histograms of simulated and experimental characteristics.

To propagate the uncertainty from the subcellular to the cellular level, for each subject, we took 500 samples of the posterior distribution for our sarcomere numbers at week 8, applied our linear model to these samples, and obtained a simulated distribution, which we compared to the posterior distribution of our experimental myocyte lengths at week 8. To quantify the agreement between the simulated and experimental myocyte lengths, we used the overlap coefficient [24], i.e., the percentage agreement between both histograms, $\sum_i^{n_{\text{bins}}} \min(f_i^{\text{sim}}, f_i^{\text{exp}})/n_{\text{smp}}$, where $n_{\text{bins}} = 31$ is the number of bins, f_i^{sim} and f_i^{exp} are the simulated and experimental frequencies of the i-th bin, and $n_{\text{smp}} = 500$ is the total number of samples, i.e., the collective sum of frequencies across all bins.

To account for the uncertainty in our cellular measurements, we correlated the longitudinal and transverse growth multipliers, $\vartheta^{\parallel} = \exp(b_{\text{ml}} t)$ and $\vartheta^{\perp} = \exp(b_{\text{mw}} t)$, to the parameters b_{ml} and b_{mw} from the experimentally measured histology from Eq. (3). These expressions arise naturally from normalizing the myocyte length and width, $\text{ml}(t) = \exp(a_{\text{ml}}) \exp(b_{\text{ml}} t)$ and $\text{mw}(t) = \exp(a_{\text{mw}}) \exp(b_{\text{mw}} t)$, from Eq. (1) by their initial values, $\exp(a_{\text{ml}})$ and $\exp(a_{\text{mw}})$.

To propagate the uncertainty from the cellular to the organ level, for each subject, we took the last 500 samples of b_{ml} and b_{mw} from the Hamiltonian Monte Carlo chain. Instead of performing a single simulation for each of the 500 samples, we trained a Gaussian process regression [39,40] to predict the end diastolic volume of the simulation [38]. For each subject, in the expected range of uncertainty, we performed n = 10 simulations for training and an additional n = 5 simulations for validation. Since intermedi-
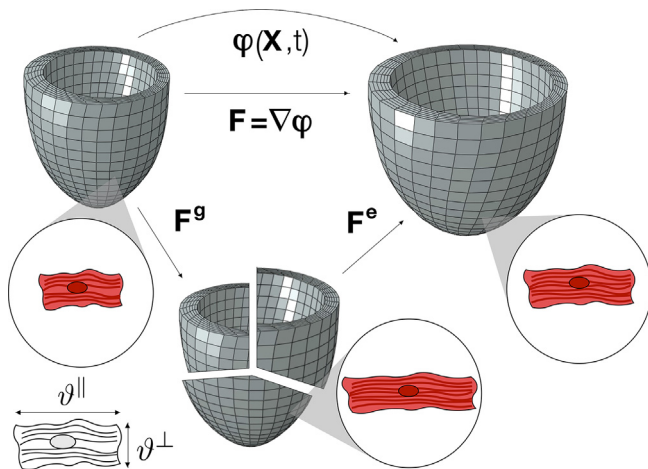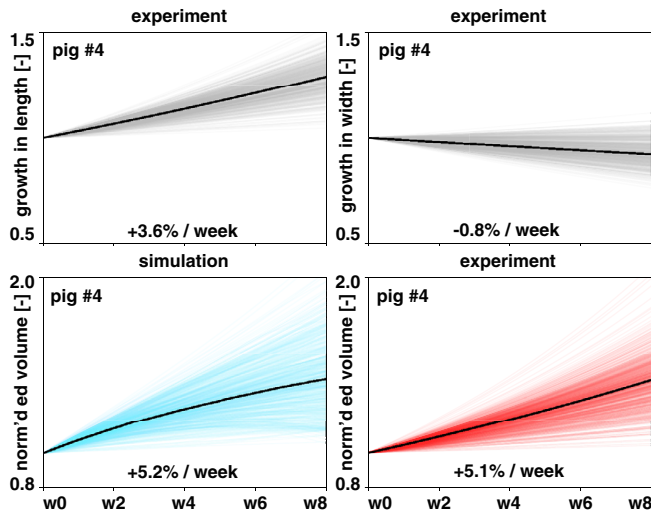
Fig. 4. Growth in myocyte length and width, and simulated and experimental changes in normalized end diastolic volumes. Gray lines represent uncertainties in myocyte measurements, blue lines uncertainties propagated into end diastolic volume simulations, red lines uncertainties in end diastolic volume measurements, and black lines the median for each case. (For interpretation of the references to colour in this figure legend, the reader is referred to the web version of this article.)

ate steps towards the final solution are also valid data points, we gathered 301 unique points for training and 151 for validation for each subject. After training the Gaussian process regression on the training set, the root mean squared error on the validation set was less than 1.3% with respect to the baseline volume for all pigs. We then used the 500 samples for b_{ml} and b_{mw} and evaluated the longitudinal and transverse growth multipliers $\vartheta^{\parallel}$ and $\vartheta^{\perp}$ at 101 time points between weeks 0 and 8 to generate a total of 50,500 values of $\vartheta^{\parallel}$ and $\vartheta^{\perp}$ for each subject. We propagated these values through a Gaussian process regression and obtained a simulated distribution of end diastolic volumes, which we compared to the experimentally measured end diastolic volumes from echocardiography. To quantify the agreement between the simulated and experimental end diastolic volumes, we used the overlap coefficient [24], i.e., the percentage agreement between both histograms, $\sum_{i}^{n_{bins}} \min(f_i^{sim}, f_i^{exp})/n_{smp}$, again using a total of $n_{bins} = 31$ bins and $n_{smp} = 500$ samples. Fig. 4 illustrates the uncertainty propagation within our growth model and its comparison to the experimental measurements for one animal, pig #4.

3. Results

3.1. Sarcomere numbers increase with volume overload

Table 1 summarizes our recorded sarcomere numbers and sarcomere lengths at baseline and throughout the follow up period of

Table 1
Changes in sarcomere number sn, sarcomere length sl, myocyte length ml, and myocyte width mw in response to left ventricular volume overload. Results are summarized as mean ± standard deviation.

	w0	w2	w4	w6	w8	Δ/week
sn	47.50	49.91	50.36	49.97	62.07	+3.83%
[–]	±11.67	±9.96	±10.76	±11.62	±16.35	
sl	1.75	1.78	1.75	1.76	1.77	+0.14%
[μm]	±0.15	±0.13	±0.10	±0.10	±0.11	
ml	85.45	84.77	86.85	84.38	107.75	+3.26%
[μm]	±22.30	±17.17	±18.45	±18.93	±26.57	
mw	13.67	13.04	14.19	13.85	12.98	−0.63%
[μm]	±3.73	±3.20	±2.96	±2.92	±3.01	

eight weeks of volume overload. Altogether, we collected n = 404 measurements of sarcomere number and n = 930 measurements of sarcomere length. The average sarcomere number per myocyte increased from 47.50 ± 11.67 to 62.07 ± 16.35, with a relatively constant sarcomere number throughout the first six weeks and a steep increase between weeks 6 and 8. At the same time, the average sarcomere length remained virtually constant at 1.76 μm, varying marginally between minimum values of 1.75 ± 0.15 μm and maximum values of 1.78 ± 0.13 μm.

Figs. 5 and 6 illustrate the sarcomere number and length measured in all six animals in response to eight weeks of ventricular volume overload. The gray dots represent the n = 404 and n = 930 individual measurements, the solid black lines represent their medians, and dashed black lines their 95% confidence intervals. The average sarcomere number in Fig. 5 increased markedly, by +3.83%/week, with a rapid increase between weeks 6 and 8. The direct comparison between the six animals illustrates the inter-animal variation; pig #2 displayed the largest increase in sarcomere number with +5.8%/week, pig #1 the smallest with +3.1%/week. The average sarcomere length in Fig. 6 varied only margin-
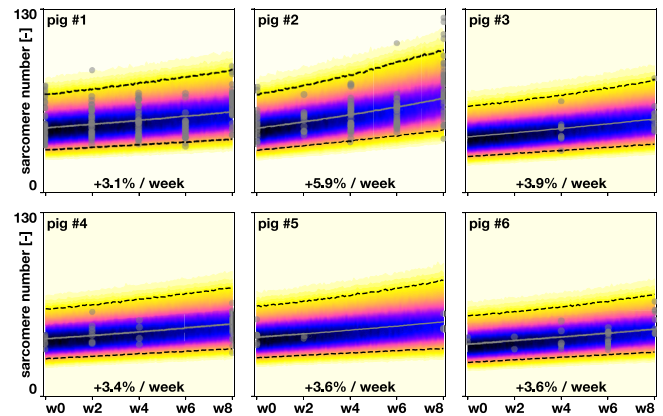

Fig. 5. Changes in sarcomere number in response to left ventricular volume overload. Gray dots represent n = 404 individual measurements of sarcomere numbers, solid gray lines represent their medians, and dashed black lines their 95% confidence intervals. Color contours from black to white highlight the probability density from high to low. (For interpretation of the references to colour in this figure legend, the reader is referred to the web version of this article.)
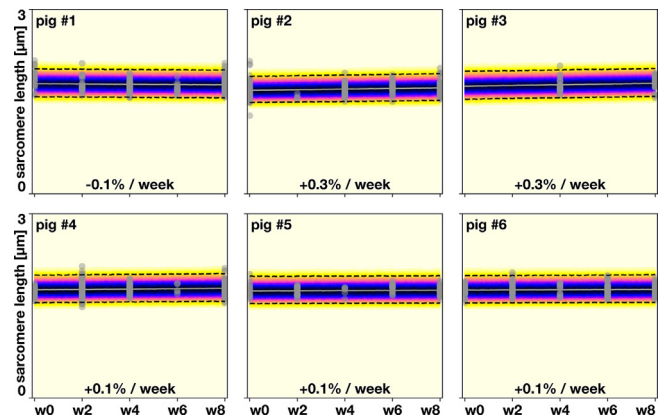

Fig. 6. Changes in sarcomere length in response to left ventricular volume overload. Gray dots represent n = 930 individual measurements of sarcomere lengths, solid gray lines represent their medians, and dashed black lines their 95% confidence intervals. Color contours from black to white highlight the probability density from high to low. (For interpretation of the references to colour in this figure legend, the reader is referred to the web version of this article.)

ally, by +0.14%/week, and, as the small 95% confidence intervals indicate, remained tightly regulated within its physiological range despite ventricular overload. Pigs #2 and #3 displayed the largest increase in sarcomere length with +0.3%/week, pig #1 displayed a small decrease with −0.2%/week.

3.2. Myocyte lengths increase with volume overload

Table 1 summarizes the results of our recorded myocyte morphologies throughout the follow up period of eight weeks of volume overload. Altogether, we collected n = 460 measurements of myocyte length and width. The average myocyte length increased, from 85.45 ± 22.30 μm to 107.75 ± 26.57 μm, with a relatively constant myocyte length throughout the first six weeks and a steep increase between weeks 6 and 8. At the same time, the average myocyte width remained virtually constant at 13.55 μm, varying marginally between minimum values of 12.98 ± 3.01 μm and maximum values of 14.19 ± 2.92 μm.

Figs. 7 and 8 illustrate the myocyte length and width measured in all six animals in response to eight weeks of ventricular volume overload. The gray dots represent the n = 460 individual measurements, the solid black lines represent their medians, and dashed black lines their 95% confidence intervals. The average myocyte length in Fig. 7 increased markedly, by +3.26%/week, with a rapid increase between weeks 6 and 8. The direct comparison between the six animals illustrates the inter-animal variation; pig #2 displayed the largest increase in myocyte length with +6.8%/week, pig #5 the smallest with +2.3%/week. The average myocyte width in Fig. 8 varied only marginally, by −0.63%/week. Pig #2 displayed the largest increase in myocyte width with +0.7%/week, pig #6 displayed the largest decrease with −0.9%/week.

3.3. End-diastolic volumes increase with volume overload

Table 2 summarizes the results of our echocardiography analysis at baseline and throughout the follow up period of eight weeks of volume overload. Altogether, we collected n = 28 measurements of end diastolic and end systolic volume, ejection fraction, and left ventricular mass. The average end diastolic and end systolic volumes increased from 67.9 ± 20.6 ml and 30.2 ± 9.5 ml at baseline to 100.2 ± 17.9 ml and 51.3 ± 9.0 ml at week eight. This resulted in a decrease in ejection fraction from 55.6 ± 4.9% to 47.7 ± 9.5%.
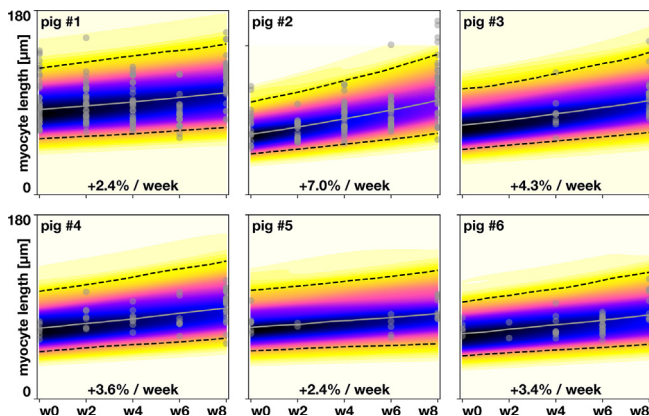

Fig. 7. Changes in myocyte length in response to left ventricular volume overload. Gray dots represent n = 460 individual measurements of myocyte lengths, solid gray lines represent their medians, and dashed black lines their 95% confidence intervals. Color contours from black to white highlight the probability density from high to low. (For interpretation of the references to colour in this figure legend, the reader is referred to the web version of this article.)

Fig. 8. Changes in myocyte width in response to left ventricular volume overload. Gray dots represent n = 460 individual measurements of myocyte width, solid gray lines represent their medians, and dashed black lines their 95% confidence intervals. Color contours from black to white highlight the probability density from high to low. (For interpretation of the references to colour in this figure legend, the reader is referred to the web version of this article.)
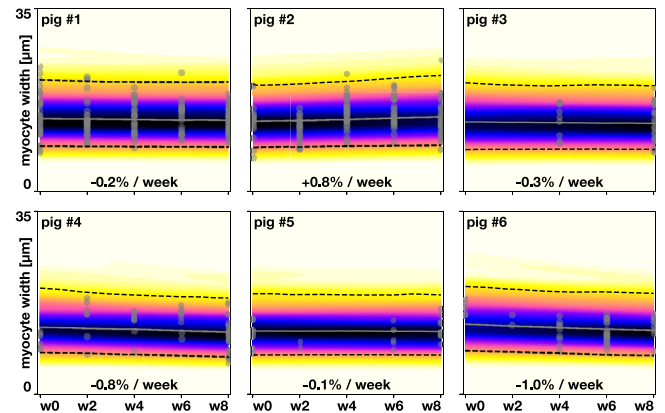
Table 2
Changes in end diastolic volume ed, end systolic volume es, ejection fraction ef, and left ventricular mass m in response to left ventricular volume overload. Results are summarized as mean ± standard deviation.

	w0	w2	w4	w6	w8	Δ/week
ed	67.9	71.3	77.7	86.8	100.2	+5.95%
[ml]	±20.6	±11.0	±9.5	±13.4	±17.9	
es	30.2	34.4	40.1	44.6	51.3	+8.73%
[ml]	±9.5	±7.2	±7.8	±5.7	±9.0	
ef	55.6	52.0	48.4	47.8	47.7	−1.78%
[%]	±4.9	±6.4	±7.3	±7.7	±9.5	
m	59.6	71.8	78.7	92.1	106.7	+9.88%
[g]	±12.2	±13.6	±16.8	±21.7	±26.9	

At the same time, the mass almost doubled from 59.6 ± 12.2 g to 106.7 ± 26.9 g.

Fig. 9 illustrates the end diastolic volume in all six animals in response to eight weeks of ventricular volume overload. The gray dots represent the n = 28 individual measurements, the solid black lines represent their medians, and dashed black lines their 95% confidence intervals. The average end diastolic volume increased by +5.95%/week, with a rapid increase between weeks 6 and 8. The direct comparison between the six animals illustrates the inter-animal variation; pig #3 displayed the largest increase in end diastolic volume with +12.3%/week, pig #1 the smallest with +2.5%/week. Since the end systolic volume increased by +8.73%/week, more rapidly that the end diastolic volume, the overall ejection fraction decreased, by −1.78%/week. Most notably, the left ventricular mass increased by 9.88%/week.

3.4. Sarcomere numbers are predictors of myocyte length

For each pig, we successfully propagated uncertainties of n = 500 sarcomere numbers from the histological measurements through our linear model and obtained simulated myocyte lengths, which we compared against our experimentally measured myocyte lengths from our biopsy histology.

Fig. 10 compares our simulated myocyte lengths from the Gaussian process regression and our experimentally measured myocyte lengths after eight weeks of left ventricular volume overload. The blue histograms represent the simulation, the red histograms the experiment. The overlap between both is a quantitative measure between the agreement of the model prediction and the experiment. The six histograms are a qualitative and quantitative illustra-
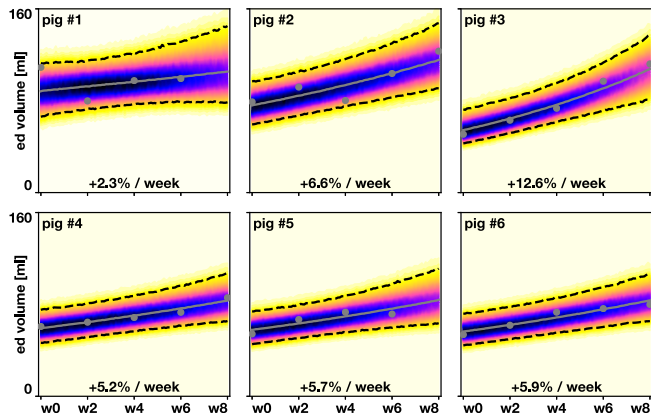
Fig. 9. Changes in end diastolic volume in response to left ventricular volume overload. Gray dots represent n = 28 individual measurements of end diastolic volume, solid gray lines represent their medians, and dashed black lines their 95% confidence intervals. Color contours from black to white highlight the probability density from high to low. (For interpretation of the references to colour in this figure legend, the reader is referred to the web version of this article.)
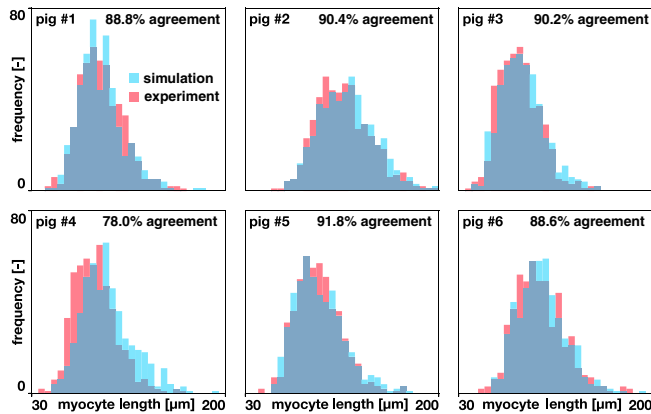

Fig. 10. Simulation and experiment of myocyte length in response to left ventricular volume overload. Blue histograms represent simulations, red histograms represent experiments, both with uncertainty; percentage agreement refers to the region shared between both histograms. The average agreement between simulation and experiment was 88%. (For interpretation of the references to colour in this figure legend, the reader is referred to the web version of this article.)

tion of the intersubject variability of cardiac growth on the cellular level. The average agreement between simulation and experiment was 88%, ranging from an excellent agreement of 91.8% for pig #5 to a very good agreement of 78.0% for pig #4. In other words, alterations in sarcomere number alone explain myocyte lengthening by 88%. Taken together, Fig. 10 suggests that the serial sarcomere number is the major determinant of myocyte length.

3.5. Myocyte lengths are predictors of ventricular dilation

For each pig, we successfully propagated uncertainties of n = 500 myocyte lengths and widths from the histological measurements through the Gaussian process regression and obtained simulated end diastolic volumes, which we compared against our experimentally measured end diastolic volumes from echocardiography.

Table 3 summarizes our individually identified subject-specific material parameters for the Holzapfel-Ogden model. We consistently identified stiffness parameters of the same order of magnitude, with a mean isotropic stiffness of $a = 80.2$ Pa, and mean fiber and sheet stiffnesses of $a_f = 264.5$ Pa, $a_s = 36.7$ Pa, and $a_{fs} = 21.5$ Pa. Interestingly, the standard deviations for these four

Table 3
Subject-specific material parameters identified individually for each pig using the Holzapfel-Ogden model.

pig	a [Pa]	b [–]	a_f [Pa]	b_f [–]	a_s [Pa]	b_s [–]	a_{fs} [Pa]	b_{fs} [–]
#1	69.6	4.34	229.6	8.34	31.8	7.23	18.7	1.78
#2	89.5	5.17	295.0	9.93	40.9	8.61	24.0	2.11
#3	74.9	4.34	247.1	8.34	34.3	7.23	20.1	1.78
#4	62.9	4.32	207.4	8.29	28.8	7.19	16.9	1.77
#5	101.1	5.80	333.4	11.13	46.3	9.65	27.2	2.37
#6	83.2	4.40	274.5	8.44	38.1	7.32	22.3	1.80
mean	80.2	4.73	264.5	9.08	36.7	7.87	21.5	1.94
std	13.9	0.62	46.0	1.19	6.4	1.03	3.8	0.25

parameters varied in a narrow range between 17.3% and 17.7% of their means.

Table 4 summarizes the range of uncertainties in myocyte lengths $\vartheta^\parallel$ and myocyte widths $\vartheta^\perp$ that we used to calculate the growth tensor, $\boldsymbol{F}^g = \vartheta^\parallel \boldsymbol{n} \otimes \boldsymbol{n} + \vartheta^\perp [\boldsymbol{I} - \boldsymbol{n} \otimes \boldsymbol{n}]$, to propagate uncertainties from our histological measurements into our transversely isotropic growth simulations.

Fig. 11 illustrates representative simulation of the end diastolic volumes in response to left ventricular volume overload. The example shows the growing left ventricle at end diastole at weeks 0, 2, 4, 6, and 8, here simulated with the median myocyte length $\vartheta^\parallel$ and myocyte width $\vartheta^\perp$ for pig #4 according to Fig. 4. The final simulated normalized end diastolic volume at week 8 of 1.44 enters the blue histogram of simulated volumes in Fig. 12 as one data point for pig #4. For all six animals, we simulated $n_{smp} = 500$ normalized end diastolic volumes using the rage of myocyte lengths $\vartheta^\parallel$ and myocyte widths $\vartheta^\perp$ in Table 4.

Table 5 compares the computationally simulated changes in normalized end diastolic volumes against the experimentally measured normalized end diastolic volumes. The computationally simulated average end diastolic volume increased by +8.55% per week, compared to the experimentally measured increase of +6.42% per week. This resulted in a simulated total volume increase of 57% throughout the period of eight weeks compared to the experimentally measured increase of 51%. The simulated average weekly

Table 4
Parameter ranges for uncertainty propagation simulations.

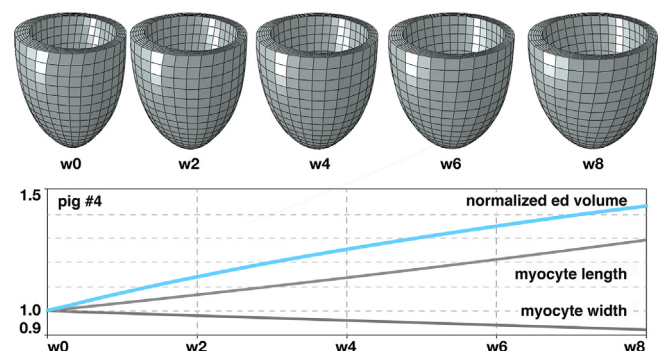| pig	$\vartheta^\parallel$	$\vartheta^\perp$	pig	$\vartheta^\parallel$	$\vartheta^\perp$
#1	1.04–1.34	0.87–1.15	#4	1.05–1.56	0.76–1.12
#2	1.31–1.81	0.91–1.29	#5	0.92–1.55	0.79–1.38
#3	1.04–1.88	0.75–1.27	#6	1.00–1.64	0.69–1.12

Fig. 11. Simulation of end diastolic volumes in response to left ventricular volume overload. The example shows the growing left ventricle at end diastole from week 0 to week 8, here simulated with the median myocyte length $\vartheta^\parallel$ and myocyte width $\vartheta^\perp$ according to Fig. 4.
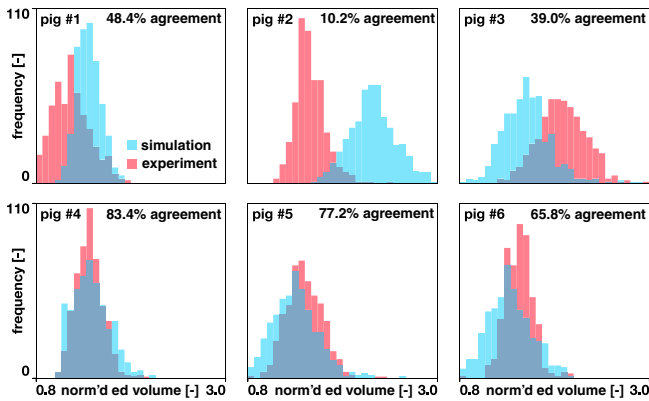
Fig. 12. Simulation and experiment of normalized end diastolic volume in response to left ventricular volume overload. Blue histograms represent simulations, red histograms represent experiments, both with uncertainty; percentage agreement refers to the region shared between both histograms. The average agreement between simulation and experiment was 54%. (For interpretation of the references to colour in this figure legend, the reader is referred to the web version of this article.)

Table 5
Changes in normalized end diastolic volumes from simulation and experiment. Results are summarized as mean values.

pig	Δed	w0	w2	w4	w6	w8	Δ/week
#1	sim	1.00	1.11	1.21	1.31	1.41	+5.13%
	exp	1.00	1.04	1.09	1.15	1.20	+2.54%
#2	sim	1.00	1.28	1.58	1.91	2.26	+15.71%
	exp	1.00	1.11	1.23	1.37	1.52	+6.56%
#3	sim	1.00	1.15	1.29	1.44	1.58	+7.24%
	exp	1.00	1.19	1.41	1.67	1.99	+12.38%
#4	sim	1.00	1.14	1.25	1.35	1.44	+5.51%
	exp	1.00	1.09	1.19	1.30	1.42	+5.24%
#5	sim	1.00	1.09	1.18	1.27	1.35	+4.37%
	exp	1.00	1.10	1.20	1.32	1.46	+5.70%
#6	sim	1.00	1.12	1.22	1.31	1.38	+4.78%
	exp	1.00	1.10	1.22	1.35	1.49	+6.09%
overall	sim	1.00	1.15	1.29	1.43	1.57	+8.55%
	exp	1.00	1.11	1.22	1.36	1.51	+6.42%

increase ranged from +4.37% for pig #5 to +15.71% for pig #2. The experimental average weekly increase ranged from +2.54% for pig #1 to +12.38% for pig #3.

Fig. 12 compares our simulated end diastolic volumes from the Gaussian process regression and our experimentally measured normalized end diastolic volumes after eight weeks of left ventricular volume overload. The blue histograms represent the simulation, the red histograms the experiment. The overlap between both is a quantitative measure between the agreement of the model prediction and the experiment. The six histograms are a qualitative and quantitative illustration of the intersubject variability of cardiac growth. The average agreement between simulation and experiment was 54%, ranging from an excellent agreement of 83.4% for pig #4 to a poor agreement of 10.2% for pig #2, which was the largest pig of the study with an initial weight of 56.1 kg. Assuming pig #2 is an outlier, the agreement for the remaining five pigs is 62.7%. In other words, for pigs #1, #3, #4, #5, and #6, alterations in myocyte morphology alone explain the dilation of the ventricle by 62.7%. Taken together, Fig. 12 suggests that myocyte morphology is the major determinant of ventricular dilation.

4. Discussion

It has long been recognized that heart failure through dilated cardiomyopathy is associated with an increase in sarcomeres on the subcellular scale, myocyte lengthening on the cellular scale, and ventricular dilation on the whole organ scale. The objective of this study was to quantify the correlation between these three characteristics on more mechanistic grounds and specify to which extent alterations on the smaller scale can explain observations on the larger scale. With this in mind, we designed a longitudinal study of heart failure that combines a chronic volume overload model, continuum growth modeling, and machine learning to systematically correlate the subcellular, cellular, and organ scales. Unique to our study is the fact that we collected biopsy samples of one and the same heart at five consecutive points in time. We recorded a total of n = 404 sarcomere numbers, n = 930 of sarcomere lengths, n = 460 of myocyte lengths and widths, and n = 28 of end diastolic and systolic volumes across five points in time and observed a substantial inter-animal variability. We therefore decided to consult machine learning tools to overlay uncertainty to our measurements, and propagate this uncertainty from the subcellular to the cellular and from the cellular to the whole organ levels. This allowed us to interpret individual intra-animal alterations in view of all other animals, and solidly quantify the agreement between our computational growth model and our experimental measurements. As such, our proposed method of probing cell-organ level correlations by combining multiscale modeling and machine learning is of general interest to a broad range of living systems and even could help characterize the influence of biomaterial-based devices, injectable hydrogels, or stents on the living heart.

4.1. Volume overload triggers an increase in sarcomere number, myocyte length, and end diastolic volume

Our study revealed that chronic volume overload triggered an increase in the serial sarcomere number, myocyte length, and end diastolic volume. On the subcellular level, we observed average changes in sarcomere number of +3.83% in Table 1 illustrated in detail in Fig. 5. These ultrastructural alterations translated almost directly into altered myocyte morphologies with average chronic myocyte lengthening of +3.26% in Table 1 illustrated in detail in Fig. 7. At the same time, the length of the individual sarcomeres in Fig. 6 was tightly regulated at 1.8 μm and the myocyte thickness in Fig. 8 remained virtually unchanged at 14 μm. While this agrees well with constant sarcomere lengths reported in the literature [57], several studies report a slightly larger sarcomere length of 2.0 μm and myocyte width of 18 μm [13]. However, those values were measured in isolated cells [5], which could be less constraining than recording dimensions in intact biopsy samples as we proposed here. Notably, our rates of both sarcomere addition and myocyte lengthening were nonlinear in time with a more pronounced increase towards the end of the study as detailed in Table 1. During the last two weeks of our study, we recorded an average sarcomere increase of 12, which agrees well with experimental findings in volume overloaded rabbit hearts that reported a maximum sarcomere deposition rate of one sarcomere per myocyte per day [57]. Our myocyte lengthening of 26% within only eight weeks compares well with myocytes from failing hearts of patients with ischemic cardiomyopathy that were 40% longer than myocytes of healthy controls [13]. We recorded a myocyte length-to-width ratio of 6.3 at baseline and of 8.3 after eight weeks of chronic volume overload. These values lie well within the range of reported healthy and failing myocyte length-to-width ratios of 7.5 [3] and 11.5 [15].

On the whole organ level, our study confirmed the common understanding that a chronic volume overload induces an increase in end diastolic and systolic volumes [36], as we showed in Fig. 9. Collectively, these structural alterations resulted in a decrease of ejection fraction and a drastic increase in mass as summarized in

Table 2. Specifically, the changes in end diastolic volume and left ventricular mass were +5.95%/ week and 9.88%/ week, which resulted in a 48% increase in end diastolic volume and a 79% increase in left ventricular mass after only eight weeks. This agrees well with clinical observations [29], although the values of our eight-week long study are generally lower than those of end-stage heart failure patients [13]. In contrast, our longitudinal growth factor of $\vartheta^\parallel = 1.20$ was markedly higher than the longitudinal growth factor of $\vartheta^\parallel = 1.05$ reported in a similar continuum growth analysis over a period of seven weeks in sheep [55]. However, in that study, growth was triggered by infarct-induced ventricular dilation and the overall degree of left ventricular dilation was significantly smaller than in our current study.

4.2. Sarcomere numbers and myocyte lengths are predictors for heart failure

To systematically correlate changes in sarcomere number and myocyte morphology to cardiac dilation, we adopted a standard continuum growth model and evaluated its predictions with the help of machine learning tools. Specifically, our goal was to answer to which extent changes in the serial sarcomere number can explain chronic myocyte lengthening and, similarly, to which extent changes in myocyte length can explain ventricular dilation. To answer both questions, we used a multiscale modeling approach and fed the small scale measurements into our multiscale model to derive a large scale prediction, which we then compared to the large scale measurements [17,47,48,58].

For the elastic part of our model, our parameter identification was robust and solid as Table 3 confirms. We identified a mean isotropic stiffness of $a = 80.2$ Pa, and mean fiber and sheet stiffnesses of $a_f = 264.5$ Pa, $a_s = 36.7$ Pa, and $a_{fs} = 21.5$ Pa, all with standard deviations of less than 20%. This confirms our intuition that heart muscle tissue is strongest along the fiber direction, and agrees well with reported trends. Strikingly, these four stiffness values identified for six living pig hearts are 6, 57, 89, and 31 times softer than the original Holzapfel-Ogden parameters [22], $a = 496$ Pa, $a_f = 15193$ Pa, $a_s = 3283$ Pa, and $a_{fs} = 662$ Pa from shear tests of 3 mm-sized cubic samples of six explanted pig hearts [8], a trend that has been confirmed by several other in vivo studies in the literature [12,46].

For the growth part of our model, a major challenge was the strong inter-animal variability with one clear outlier, animal #2. For all other animals we observed a strong agreement between simulation and experiment as Table 5 confirms. Our study revealed that changes in the serial sarcomere number explain myocyte lengthening by 88% as we illustrate in detail for each animal in Fig. 10. Similarly, changes in myocyte length explain ventricular dilation by 54% as we show in Fig. 12. On average, the simulation predicted a weekly increase in end diastolic volume of +8.55%/ week, which agrees well with the experimentally observed increase of +6.42%/week.

While various studies have analyzed the effects of volume overload on sarcomere number, myocyte length, and ventricular volume [14,19,20,35], only a small number of studies have made attempts to quantify correlations between them [13]. In fact, the relative contributions of myocyte remodeling and myocyte slippage to the dilation of the ventricle remain an ongoing controversy in the quest for successful therapies to treat heart failure [14]. Probably the most quantitative correlation to date is a linear relation between chamber circumference and myocyte length in progressive heart failure in rats [54]. This study concluded that myocyte lengthening alone can account for chamber dilation in the progression to heart failure [51]. In directly correlating chamber circumference to myocyte length, however, this study ignored

the structural arrangement of myocardial fibers across the ventricular wall and implicitly assumed that myocytes elongate only along the circumferential direction. Kinematically, this model provides only an upper limit of ventricular dilation. To explain potential discrepancies between myocyte lengthening and ventricular dilation, a recent study suggested that extracellular matrix remodeling could be a significant contributor to volume overload-induced heart failure [23].

Recent reviews have begun to acknowledge the importance of computational modeling in providing additional insight into the pathological alterations of heart failure across the scales [4,51]. The very first approach to characterize growth of the heart was purely theoretical, but introduced the multiplicative decomposition of the deformation gradient into an elastic part and a growth part according to Fig. 3 [43]. Throughout the past decade, numerous groups have used and refined this approach to model eccentric and concentric cardiac growth, either through separate stretch- and stress-driven models [16,26,41] or through a single strain-based model [25]. In contrast to the simplified myocyte length versus chamber diameter model, computational models allow us to directly account for discrete fiber directions in the left ventricle [28] or across the entire heart [12], either derived from a rule-based approach [56] or registered on the geometry from diffusion tensor magnetic resonance imaging [46]. Here we have systematically included fiber heterogeneity across the ventricular wall through discrete, regionally varying fiber directions $\boldsymbol{n}$ in Eq. (4). Our histogram representations of the animal-specific correlations between sarcomere number and myocyte length in Fig. 10 and between myocyte length and ventricular dilation in Fig. 12 reveal that sarcomere numbers are an excellent predictor for myocyte lengthening, which, in turn, is a good predictor for ventricular dilation. While myocyte lengthening alone indeed explains 54% of the structural alterations associated with ventricular dilation, our study also supports the emerging view that extracellular matrix remodeling could play a relevant-although overall less important-role in heart failure. Further studies will be needed to elucidate to which extent the remaining cardiac dilation and increase in ventricular mass can be explained by myocyte hyperplasia or extracellular matrix deposition. A better understanding of the contributing factors to heart failure could have potential implications on tissue engineering functional heart muscle for cardiac repair [2] or testing of novel biomaterial-based devices for combating heart failure [42].

4.3. Limitations

This manuscript provides our first attempts to quantitatively correlate sarcomere lengths and numbers, myocyte lengths and widths, and ventricular volumes in individual animals throughout a longitudinal heart failure study. Our study has a few limitations: First, we have only monitored our animals throughout a period of eight weeks during which structural changes were initially moderate but increased more rapidly towards the end of the study. A unique aspect of our study is that we know about this temporal variation in growth because we have collected biopsy samples of the same heart at five points in time. In retrospect, we should probably have continued the study for an additional two or even four weeks. However, the hearts had already almost doubled their mass within only eight weeks which indicates a rather rapid growth. Second, while the mass of the hearts almost doubled, the animals themselves grew to a final body weight of 60.7 ± 10.7 kg and increased their mass by 31.1%. Here we focused exclusively on how changes in sarcomere number translate into changes in myocyte length and changes in end diastolic volume. In a follow up study, we are currently characterizing the naturally-induced and stretch-induced addition of sarcomeres to shed light on the relative

influence of these two phenomena. Third, in our initial cohort, we have only studied six animals. Given the relatively large inter-animal variation, the number of animals seems rather low, and we should probably increase the number of subjects in the future to explore how robustly our findings extent to a larger group. Specifically, our proposed method is sensitive to the inherent inter-animal variations in natural growth, regurgitation, and overload-induced growth. While the cell-level responses in Fig. 10 seem to be tightly regulated and less sensitive to these variations, the organ-level responses in Fig. 12 display much larger inter-animal variations, which manifest themselves in an excellent agreement for pigs #4, #5, and #6, a good agreement for pigs #1 and #3, and a poor agreement for pig #2. Including additional animals would help us to better explain the discrepancies for pig #2, and likely make our overall finding more robust. For now, to analyze and interpret our relatively sparse data, we have applied novel machine learning techniques. This allows us, for example, to interpret the individual behavior of each animal in view of the collective behavior of all animals. This technology is novel and could in itself be useful for other studies that are based on interpreting sparse data. Fourth, our study induced left ventricular volume overload in pigs through controlled regurgitation as a surrogate model for heart failure in humans. While sarcomere lengths and numbers, myocyte lengths and widths, and ventricular volumes are relatively comparable between pigs and humans, it remains to be shown how the timeline of cellular and ventricular adaptation in volume overloaded pigs translates into the timeline of heart failure in humans.

5. Conclusion

Sarcomere units within individual myocytes undergo a continuous turnover through removal and renewal. Since their turnover rate is sensitive to environmental factors, the dimensions of individual myocytes are highly plastic. Altering sarcomere turnover – and with it myocyte morphology and ventricular dimensions – could be a potential therapeutic target to attenuate or reverse the progression of heart failure. Our study provides a better quantitative understanding of the correlations between sarcomere number, myocyte length, and ventricular dilation and is an important first step in this direction.

Acknowledgments

Appendix A. Supplementary data

Table 6 summarizes the number of sarcomere numbers, sarcomere lengths, myocyte lengths, and myocyte widths we recorded for each subject at each time point. In total, we measured n = 404 sarcomere lengths, n = 930 sarcomere lengths, n = 460 myocyte lengths, and n = 460 myocyte widths. Supplementary data associated with this article can be found, in the online version, at https://doi.org/10.1016/j.actbio.2018.12.053.

References

[1] E.J. Benjamin, S.V. Salim, W.C. Clifton, A.R. Chang, S. Cheng, et al., Heart disease and stroke statistics–2018 update: a report from the American Heart Association, Circulation 137 (2018) e67–e492.

[2] O.J. Abilez, E. Tzatzalos, H. Yang, M.T. Zhao, G. Jung, A.M. Zöllner, M. Tiburcy, J. Riegler, E. Matsa, P. Shukla, Y. Zhuge, T. Chour, V.C. Chen, P.W. Burridge, I. Karakides, E. Kuhl, D. Bernstein, L.A. Couture, J.D. Gold, W.H. Zimmermann, J.C. Wu, Passive stretch induces structural and functional maturation of engineered heart muscle as predicted by computational modeling, Stem Cells 36 (2018) 265–277.

[3] M.A. Bray, S.P. Sheehy, K.K. Parker, Sarcomere alignment is regulated by myocyte shape, Cell Motililty Cytoskel. 65 (2008) 641–651.

[4] R. Chabiniok, V. Wang, M. Hadjicharalambous, L. Asner, J. Lee, M. Sermesant, E. Kuhl, A. Young, P. Moireau, M. Nash, D. Chapelle, D.A. Nordsletten, Multiphysics and multiscale modeling, data-model fusion and integration of organ physiology in the clinic: ventricular cardiac mechanics, Interface Focus 6 (2016) 20150083.

[5] Y.F. Chen, S. Said, S.E. Campbell, A.M. Gerdes, A method to collect isolated myocytes and whole tissue from the same heart, Am. J. Physiol. Heart Circ. Physiol. 293 (2007) 2004–2006.

[6] J.S. Choy, S. Leng, Y. Awakeem, K.L. Sack, Y. Dabiri, L. Zhong, J.M. Guccione, G.S. Kassab. Mechanical stretch as stimulus for growth and remodeling in mitral regurgitation (submitted for publication).

[7] Dassault Systémes, SIMULIA. 2017. Abaqus 2017, Documentation. Dassault Systémes, Rhode Island.

[8] S. Dokos, B.H. Smaill, A.A. Young, I.J. LeGrice, Shear properties of passive ventricular myocardium, Am. J. Physiol. Heart Circ. Physiol. 283 (2002) H2650–H2659.

[9] O. Frank, Zur Dynamik des Herzmuskels, J. Biol. 32 (1895) 370–447. Translation from German: Chapman CP, Wasserman EB. On the dynamics of cardiac muscle. Am. Heart J. 58 (1959) 282–317.

[10] A. Gelman, Prior distributions for variance parameters in hierarchical models, Bayesian Anal. 1 (2006) 515–534.

[11] A. Gelman, J. Hill, Data Analysis Using Regression and Multilevel/Hierarchical Models, Cambridge University Press, Cambridge, 2006.

[12] M. Genet, L.C. Lee, B. Baillargeon, J.M. Guccione, E. Kuhl, Modeling pathologies of systolic and diastolic heart failure, Ann. Biomed. Eng. 44 (2016) 112–127.

[13] A.M. Gerdes, S.E. Kellerman, J.A. Moore, K.E. Muffly, L.C. Clark, P.Y. Reaves, K.B. Malec, P.P. Mc Keown, D.D. Schocken, Structural remodeling of cardiac myocytes in patients with ischemic cardiomyopathy, Circulation 86 (1992) 426–430.

[14] A.M. Gerdes, The use of isolated myocytes to evaluate myocardial remodeling, Trends Cardiovasc. Med. 2 (1992) 152–155.

[15] A.M. Gerdes, J.M. Capasso, Structural remodeling and mechanical dysfunction of cardiac myocytes in heart failure, J. Mol. Cell Cardiol. 27 (1995) 849–856.

[16] S. Göktepe, O.J. Abilez, E. Kuhl, A generic approach towards finite growth with examples of athlete's heart, cardiac dilation, and cardiac wall thickening, J. Mech. Phys. Solids 58 (2010) 1661–1680.

[17] S. Göktepe, O.J. Abilez, K.K. Parker, E. Kuhl, A multiscale model for eccentric and concentric cardiac growth through sarcomerogenesis, J. Theor. Biol. 265 (2010) 433–442.

[18] S. Göktepe, S.N.S. Acharya, J. Wong, E. Kuhl, Computational modeling of passive myocardium, Int. J. Num. Meth. Biomed. Eng. 27 (2011) 1–12.

[19] W. Grossman, Cardiac hypertrophy: useful adaptation or pathologic process?, Am J. Med. 69 (1980) 576–584.

[20] J.W. Holmes, Candidate mechanical stimuli for hypertrophy during volume overload, J. Appl. Physiol. 97 (2004) 1453–1460.

[21] C. Holubarsch, T. Ruf, D.J. Goldstein, R.C. Ashton, W. Nickl, B. Pieske, K. Burkert, J. Ludemann, S. Wiesner, G. Hasenfuss, H. Posival, H. Just, D. Burkhoff, Ventricular hypertrophy/CHF: existence of the Frank-Starling mechanism in the failing human heart: Investigations on the organ, tissue, and sarcomere levels, Circulation 94 (1996) 683–689.

[22] G.A. Holzapfel, R.W. Ogden, Constitutive modelling of passive myocardium: a structurally based framework for material characterization, Philos. Trans. A. Math. Phys. Eng. Sci. 367 (2009) 3445–3475.

[23] K.R. Hutchinson, J.A. Stewart, P.A. Lucchesi, Extracellular matrix remodeling during the progression of volume overload-induced heart failure, J. Mol. Cell Cardiol. 48 (2010) 564–569.

[24] H.F. Inman, E.L. Bradley Jr, The overlapping coefficient as a measure of agreement between probability distributions and point estimation of the overlap of two normal densities, Commun. Stat. Methods. 18 (1989) 3851–3874.

[25] R.C.P. Kerckhoffs, J.H. Omens, A.D. McCulloch, A single strain-based growth law predicts concentric and eccentric cardiac growth during pressure and volume overload, Mech. Res. Commun. 42 (2012) 40–50.

[26] D. Klepach, L.C. Lee, J.F. Wenk, M.B. Ratcliffe, T.I. Zohdi, J.A. Navia, G.S. Kassab, E. Kuhl, J.M. Guccione, Growth and remodeling of the left ventricle: a case study of myocardial infarction and surgical ventricular restoration, Mech. Res. Comm. 42 (2012) 134–141.

[27] S. Klotz, I. Hay, M.L. Dickstein, G.-H. Yi, J. Wang, M.S. Maurer, D.A. Kass, D. Burkhoff, Single-beat estimation of end-diastolic pressure-volume relationship: a novel method with potential for noninvasive application, Am. J. Physiol. Circ. Physiol. 291 (2006) H403–H412.

[28] W. Kroon, T. Delhaas, T. Arts, P. Bovendeerd, Computational modeling of volumetric soft tissue growth: application to the cardiac left ventricle, Biomech. Model. Mechanobiol. 8 (2009) 301–309.

[29] V. Kumar, A.K. Abbas, N. Fausto, Robbins and Cotran Pathologic Basis of Disease, Elsevier Saunders, 2005.

[30] I.J. Legrice, P.J. Hunter, B.H. Smaill, Laminar structure of the heart: a mathematical model, Am. J. Physiol. 272 (1997) H2466–H2476.

[31] A. Leri, M. Rota, F.S. Pasqualini, P. Goichberg, P. Anversa, Origin of cardiomyocytes in the adult heart, Circ. Res. 116 (2015) 150–166.

[32] D. Lewandowski, D. Kurowicka, H. Joe, Generating random correlation matrices based on vines and extended onion method, J. Multivar. Anal. 100 (2009) 1989–2001.

[33] F. Li, X. Wang, X.P. Yi, A.M. Gerdes, Structural basis of ventricular remodeling: Role of the myocyte, Current Heart Failure Reports 1 (2004) 5–8.

[34] H. Mansour, P.P. de Tombe, A.M. Samarel, B. Russel, Restoration of resting sarcomere length after uniaxial static strain is regulated by protein kinase C and focal adhesion kinase, Circ Res. 94 (2004) 642–649.

[35] J.H. Omens, Stress and strain as regulators of myocardial growth, Prog. Biophys. Mol. Biol. 69 (1998) 559–572.

[36] L.H. Opie, Heart Physiology: From Cell to Circulation, Lippincott Williams & Wilkins, 2003.

[37] L.H. Opie, P.J. Commerford, B.J. Gersh, M.A. Pfeffer, Controversies in ventricular remodelling, Lancet 367 (2006) 356–367.

[38] P. Perdikaris. Gaussian processess. A hands-on tutorial.https://github.com/paraklas/GPTutorial, 2017.

[39] M. Raissi, P. Perdikaris, G. Karniadakis, Machine learning of linear differential equations using Gaussian processes, J. Comp. Phys. 348 (2017) 683–693.

[40] M. Raissi, P. Perdikaris, G. Karniadakis, Numerical Gaussian processes for time-dependent and nonlinear partial differential equations, SIAM J. Sci. Comp. 40 (2018) A172–A198.

[41] M.K. Rausch, A. Dam, S. Göktepe, O.J. Abilez, E. Kuhl, Computational modeling of growth: systemic and pulmonary hypertension in the heart, Biomech. Model. Mechanobiol. 10 (2011) 799–811.

[42] M.K. Rausch, A.M. Zöllner, M. Genet, B. Baillargeon, W. Bothe, E. Kuhl, A virtual sizing tool for mitral valve annuloplasty, Int. J. Numer. Meth. Biomed. Eng. 33 (2017) e02788.

[43] E. Rodriguez, A. Hoger, A.D. McCulloch, Stress-dependent finite growth in soft elastic tissues, J. Biomech. 27 (1994) 455–467.

[44] V.L. Roger, Epidemiology of heart failure, Circ. Res. 113 (2013) 6446–6659.

[45] B. Russel, M.W. Curtis, Y.E. Koschman, A.M. Samarel, Mechanical stress-induced sarcomere assembly for cardiac muscle growth in length and width, J. Mol. Cell. Cardiol. 48 (2010) 817–823.

[46] K.L. Sack, E. Aliotta, D.B. Ennis, J.S. Choy, G.S. Kassab, J.M. Guccione, T. Franz, Construction and validation of subject-specific biventricular finite-element models of healthy and failing swine hearts from high-resolution DT-MRI, Front. Physiol. 9 (2018) 539.

[47] F. Sahli Costabal, J. Yao, E. Kuhl, Predicting the cardiac toxicity of drugs using a novel multiscale exposure-response simulator, Comp. Meth. Biomech. Biomed. Eng. 21 (2018) 232–246.

[48] F. Sahli Costabal, J. Yao, E. Kuhl, Predicting drug-induced arrhythmias by multiscale modeling, Int. J. Numer. Meth. Biomed. Eng. 34 (2018) e2964.

[49] J. Salvatier, T.V. Wiecki, C. Fonnesbeck, Probabilistic programming in Python using PyMC3, Peer J. Comput. Sci. 2 (2016) e55.

[50] J.W. Sanger, J.C. Ayoob, P. Chowrashi, D. Zurawski, J.M. Sanger, Assembly of myofibrils in cardiac muscle cells, Adv. Exp. Med. Biol. 481 (2000) 89–105.

[51] O.V. Savinova, A.M. Gerdes, Myocyte changes in heart failure, Heart Fail. Clin. 8 (2012) 1–6.

[52] E.H. Starling, Linacre Lecture on the Law of the Heart, Longmans, London, England, 1918.

[53] J.A. Spudich, Hypertrophic and dilated cardiomyopathy: four decades of basic research on muscle lead to potential therapeutic approaches to these devastating genetic diseases, Biophys. J. 106 (2014) 1236–1249.

[54] T. Tamura, T. Onodera, S. Said, M.A. Gerdes, Correlation of myocyte lengthening to chamber dilation in the spontaneously hypertensive heart rat, J. Mol. Cell. Cardiol. 30 (1998) 2175–2181.

[55] A. Tsamis, A. Cheng, T.C. Nguyen, F. Langer, D.C. Miller, E. Kuhl, Kinematics of cardiac growth – in vivo characterization of growth tensors and strains, J. Mech. Behavior Biomed. Mat. 8 (2012) 165–177.

[56] J. Wong, E. Kuhl, Generating fiber orientation maps in human heart models using Poisson interpolation, Comp. Meth. Biomech. Biomed. Eng. 17 (2014) 1217–1226.

[57] M. Yoshida, E. Sho, H. Nanjo, M. Takahashi, M. Koboyashi, K. Kawamura, M. Honma, M. Komatsu, A. Sugita, M. Yamauchi, T. Hosoi, Y. Ito, H. Matsuda, Weaving hypothesis of cardiomyocyte sarcomeres, Am. J. Pathol. 176 (2010) 660–678.

[58] K.M. Wisdom, S.L. Delp, E. Kuhl, Use it or lose it: multiscale skeletal muscle adaptation to mechanical stimuli, Biomech. Model. Mechanobiol. 14 (2015) 195–215.

[59] A.M. Zöllner, O.J. Abilez, M. Böl, E. Kuhl, Stretching skeletal muscle – Chronic muscle lengthening through sarcomerogenesis, PLoS ONE 7 (2012) e45661.